INTERNATIONAL JOURNAL FOR NUMERICAL METHODS IN FLUIDS, VOL. 21, 499–522 (1995)

# AN INVESTIGATION OF ARTIFICIAL DISSIPATION FOR THE CELL-VERTEX FINITE VOLUME METHOD

J. A. MACKENZIE

*Department of Mathematics, University of Strathclyde, Livingstone Tower, 26 Richmond Street, Glasgow, U.K.*

SUMMARY

This paper is concerned with an investigation of artificial dissipation models that are used with the cell-vertex finite volume approximation of the compressible Euler and Navier–Stokes equations. Based on the observation that first and second-order upwind schemes can be written as a central discretization plus an appropriately scaled dissipative flux, a matrix scaling of second and fourth-differences is implemented in an artificial dissipation model that also uses a procedure to limit the applicability of shock-capturing dissipation. Analysis of the model and the associated boundary conditions is given to determine the effect on accuracy. Numerical results are given for transonic Euler flow past a NACA0012 aerofoil profile which demonstrate the improved shock-capturing capability of the model. Results for laminar subsonic viscous flow over a flat plate show that the matrix-dissipation model reduces the amount of spurious artificial dissipation within boundary layers.

KEY WORDS: cell-vertex; finite volume; artificial viscosity

## 1. INTRODUCTION

The accurate solution of the steady compressible Euler and Navier–Stokes equations is a major challenge for any numerical method. The main computational problem is the monotonic resolution of discontinuous or very steep interior layers such as shocks and shear layers, whilst maintaining accuracy where the solution is smooth, for instance in boundary layers.

For problems with strong shocks, finite volume methods appear to be the method of choice due to their inherent conservation properties. In this paper we consider centred finite volume approximations which require some form of artificial dissipation to capture shocks and to damp high-frequency solution components. In particular, we concentrate on a cell-vertex formulation where the unknowns are located at the vertices of the quadrilateral grid cells. The particular cell-vertex method was originally proposed for the Euler equations by Ni[1] and Hall[2] and was analysed by Morton and Paisley,[3] who also successfully applied shock-fitting techniques for transonic problems. The method has been extended to the compressible Navier–Stokes equations and competitive results have been obtained for a series of test problems.[4–6]

The artificial dissipation model used in Crumpton *et al.*[4] consists of a non-linear blend of second and fourth-differences based on the model of Jameson.[7] This model has been applied to many central discretisations of the Euler and Navier–Stokes equations and has been modified and analysed in Reference 8 and 9. However, the original model performs poorly in some circumstances since the model is scalar in nature. For example, in inviscid transonic flow, excessive second-difference dissipation results in normal shock profiles being captured in three to five mesh cells. This compares unfavourably with the performance of upwind methods which usually capture normal shocks in two or three mesh cells. For high Reynolds number Navier–Stokes calculations, excessive fourth-

CCC 0271–2091/95/060499–24

*Received August 1993*
*Revised March 1995*

difference dissipation can be introduced normal to solid boundaries.[10] This leads to artificially thickened boundary layers and inaccurate drag prediction. Modifications of Jameson's model have been recently been proposed that scale the artificial dissipation terms by a matrix which has been derived from symmetric formulations of first-order upwind methods.[11,12] The authors report an improvement in solution accuracy at the price of a slight increase in CPU time.

The purpose of this paper is to investigate an artificial dissipation model based on a matrix-scaled blend of second and fourth-differences that also uses a procedure to limit the application of shock-capturing dissipation. In addition, we analyse the smoothing characteristics of the artificial dissipation boundary conditions. By examining the different contributions to the flux balance of the nodal and cell residuals for Euler and Navier–Stokes test problems we are able to see the beneficial effect of these modifications of the artificial dissipation model. The layout of this paper is as follows: in Section 2 we give the governing equations for two-dimensional compressible gas flow and in Sections 3 and 4 we present the cell-vertex discretisation and iterative solution procedure. In Section 5 we describe and analyse the artificial dissipation model used in Crumpton *et al.*[4] In Section 6 we consider a matrix-scaled dissipation model which also incorporates a shock-detection procedure. We present numerical results in Section 7 using the new model. Finally, we make some conclusions in Section 8.

## 2. THE GOVERNING EQUATIONS

The Navier–Stokes equations describing steady, two-dimensional, compressible flow are written in conservation form as

$$\nabla.(\mathbf{f}(\mathbf{w}, \nabla\mathbf{w}), \mathbf{g}(\mathbf{w}, \nabla\mathbf{w})) = \mathbf{0}, \quad (x, y) \in \Omega. \tag{1}$$

The vector of conserved variables and the flux functions have the following non-dimensionalized form

$$\mathbf{w} = \begin{pmatrix} \rho \\ \rho u \\ \rho v \\ \rho E \end{pmatrix}, \qquad \mathbf{f}^I = \begin{pmatrix} \rho u \\ \rho u^2 + p \\ \rho uv \\ \rho uH \end{pmatrix}, \qquad \mathbf{g}^I = \begin{pmatrix} \rho u \\ \rho uv \\ \rho v^2 + p \\ \rho vH \end{pmatrix}, \tag{2}$$

$$\mathbf{f}^V = \begin{pmatrix} 0 \\ -\tau_{xx} \\ -\tau_{xy} \\ -u\tau_{xx} - v\tau_{xy} + q_x \end{pmatrix}, \qquad \mathbf{g}^V = \begin{pmatrix} 0 \\ -\tau_{xy} \\ -\tau_{yy} \\ -u\tau_{xy} - v\tau_{yy} + q_y \end{pmatrix}, \tag{3}$$

where

$$\mathbf{f}(\mathbf{w}, \nabla\mathbf{w}) = \mathbf{f}^I(\mathbf{w}) + \mathbf{f}^V(\mathbf{w}, \nabla\mathbf{w}) \quad \text{and} \quad \mathbf{g}(\mathbf{w}, \nabla\mathbf{w}) = \mathbf{g}^I(\mathbf{w}) + \mathbf{g}^V(\mathbf{w}, \nabla\mathbf{w}).$$

Here, $\rho$, $u$, $v$, $p$, $E$ and $H$ denote the density, the two Cartesian components of velocity, the pressure, the total specific energy and the total specific enthalpy respectively. The deviatoric stress and heat conduction terms are given by

$$\tau_{xx} = \frac{2\mu}{3Re}\left(2\frac{\partial u}{\partial x} - \frac{\partial v}{\partial y}\right), \tag{4}$$

$$\tau_{xy} = \frac{\mu}{Re}\left(\frac{\partial u}{\partial y} + \frac{\partial v}{\partial x}\right), \tag{5}$$

$$\tau_{yy} = \frac{2\mu}{3Re}\left(2\frac{\partial v}{\partial y} - \frac{\partial u}{\partial x}\right), \tag{6}$$

$$q_x = -\frac{\mu}{(\gamma - 1)M_\infty^2 RePr}\frac{\partial T}{\partial x}, \tag{7}$$

$$q_y = -\frac{\mu}{(\gamma - 1)M_\infty^2 RePr}\frac{\partial T}{\partial y}, \tag{8}$$

where $\gamma$, $Re$, $Pr$ and $M_\infty$ denote the adiabatic constant, the Reynolds number, the Prandtl number and the freestream Mach number respectively. The laminar viscosity, $\mu$, is assumed to vary with temperature according to Sutherland's law. The equation system is closed by assuming an ideal gas law which gives

$$E = \frac{p}{\rho(\gamma - 1)} + \tfrac{1}{2}(u^2 + v^2). \tag{9}$$

The domain, $\Omega$, is assumed to be an open, connected subset of $\mathbb{R}^2$ with boundary $\partial\Omega$. Since our main interest is in external flows, $\Omega$ should be infinite; but for computational purposes it is truncated and appropriate far-field boundary conditions introduced. We assume that a steady solution exists that satisfies an integrated form of (1), namely

$$\oint_{\partial\Omega_\alpha} (\mathbf{f}\, dy - \mathbf{g}\, dx) = \mathbf{0} \quad \forall \Omega_\alpha \subset \Omega, \tag{10}$$

where $\Omega_\alpha$ is any sub-region of $\Omega$.

## 3. THE CELL-VERTEX DISCRETIZATION

We assume that the domain $\Omega$ can be partitioned by a set of non-overlapping, convex quadrilateral cells such that $\bar{\Omega} = \cup_\alpha \bar{\Omega}_\alpha$. This partition of the domain will be called the *primary grid*. The finite volume discretization of (10) is obtained using a quadrature rule to approximate the boundary integral for each $\Omega_\alpha$. For cell-vertex formulations of the finite volume method the discrete solution vector $\mathbf{W}_{i,j}$ is held at the vertices of the primary grid cells and in this paper the integration of inviscid fluxes along each cell edge is approximated using the trapezoidal rule.

To integrate the viscous flux functions we first need an approximation of $\nabla \mathbf{w}$. In this paper the gradient is approximated at the midpoint of each cell edge using a procedure given in Reference 4. Thereafter, the viscous flux boundary integral is approximated using the mid-point rule. Summing the approximations of the inviscid and viscous flux integrations and dividing by the cell volume we get the cell residual

$$\mathbf{R}_\alpha(\mathbf{W}) := \frac{1}{V_\alpha}\sum_{i=1}^{4}\left\{\left[\tfrac{1}{2}(\mathbf{F}_i^I + \mathbf{F}_{i+1}^I) + \mathbf{F}_{i+\frac{1}{2}}^V\right](y_{i+1} - y_i) - \left[\tfrac{1}{2}(\mathbf{G}_i^I + \mathbf{G}_{i+1}^I) + \mathbf{G}_{i+\frac{1}{2}}^V\right](x_{i+1} - x_i)\right\}, \tag{11}$$

where $\mathbf{F}_i^I$ and $\mathbf{F}_{i+\frac{1}{2}}^V$ denote the approximations of the inviscid fluxes and viscous fluxes at $\mathbf{x}_i$ and $\mathbf{x}_{i+\frac{1}{2}}$ respectively. The residual for cell $\Omega_\alpha$ involves the twelve points shown in Figure 1. The lack of compactness of the stencil is due to the discretisation of the viscous fluxes and is the price that is paid for the four point compact discretisation of the inviscid terms. With the volume weighted scaling, $\mathbf{R}_\alpha$ represents the rate of change of the average of $\mathbf{W}$ in $\Omega_\alpha$ for the unsteady problem; for the

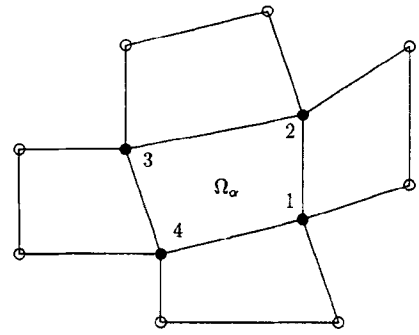


Figure 1. Geometric configuration of flow variables for the conservation cell $\Omega_\alpha$; • inviscid and viscous fluxes and ○ viscous fluxes

steady problem the aim is to drive these residuals to zero. It should be emphasized that the inviscid and viscous fluxes are integrated around the same control volume to give a consistent cell residual centred on the cells of the primary grid.

## 4. SOLUTION PROCEDURE

Having established the definition of a set of cell-based residual $\mathbf{R}_\alpha$ based on (11), it remains to describe the solution procedure to determine $\mathbf{W}$. Obviously we would expect the number of cell residuals equations to match the total number of unknowns but this requires a careful treatment with the cell-vertex method as each residual equation is associated with a cell of the primary grid and not a nodal unknown. As in References 4 and 6, we adopt the procedure of setting combinations of cell residuals to zero using a generalized Lax–Wendroff scheme to distribute contributions from each cell residual to its four corners to produce a 'node-based' residual

$$\mathbf{N}_{i,j}(\mathbf{W}) := \frac{\sum_{\alpha=1}^{p} V_\alpha D_{\alpha,(i,j)} \mathbf{R}_\alpha}{\sum_{\alpha=1}^{p} V_\alpha}, \tag{12}$$

where $p$ is the number of cells meeting at node $(i, j)$, and normally $p=4$. The exact form of the Lax–Wendroff distribution matrices, $D_{\alpha,(i,j)}$, can be found in Reference 4. The solution $\mathbf{W}$ is found using Richardson relaxation on the nodal residual equations giving the iteration

$$\mathbf{W}_{i,j}^{n+1} = \mathbf{W}_{i,j}^{n} - \omega_{i,j} \frac{\sum_{\alpha=1}^{p} (V_\alpha D_{\alpha,(i,j)} \mathbf{R}_\alpha)}{\sum_{\alpha=1}^{p} V_\alpha}, \tag{13}$$

where $\omega_{i,j}$ is a node based relaxation parameter. The resulting Lax–Wendroff iteration, through its use of the Jacobian matrices, represents a crude way of associating each unknown at a vertex with the cells which are in some sense upwind of it. At convergence a matrix-weighted combination of residuals is set to zero and in general we cannot deduce that the Lax–Wendroff procedure sets the cell residuals to zero. Not surprisingly, artificial dissipation also plays a large part in determining the exact flux balance at convergence.

## 5. NUMERICAL DISSIPATION

There are two main reasons why we need to use artificial dissipation with the cell-vertex finite volume method. First, the discretisation for both inviscid and viscous problems admits a chequer-

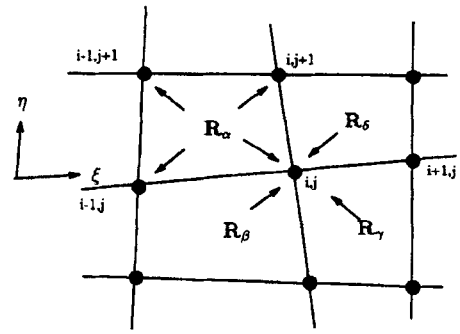


Figure 2. Distribution of the cell residual $\mathbf{R}_\alpha$ to the four cell vertices, and of the four cell residuals to the update at the vertex $i, j$

board spurious solution mode. Unfortunately, the Lax–Wendroff distribution of the cell residuals to form a nodal-residual does not introduce any damping of these high frequency modes which are therefore only checked by the imposition of boundary conditions. This control is often very weak and results in slow convergence of the time-stepping procedure. The second problem is caused by cells that are crossed by shocks. The use of the trapezoidal rule to approximate the integral of a discontinuous flux results in a large local error in the cell flux balance. Unless a careful distribution of cell residuals is performed, a process which can be done for the one-dimensional Euler equations,[13] then some form of shock-capturing artificial dissipation is necessary to prevent oscillations and possible instabilities.

The artificial dissipation model used in References 4 and 6 is based on the model by Jameson *et al.*[7]. Using the notation $\delta_\xi^2$ and $\delta_\eta^2$ to denote second-difference operators along the body-fitted coordinate lines, and referring to Figure 2, the distribution of the artificial viscosity vector from cell $\Omega_\alpha$ to node $(i, j)$ is given by

$$A_{\alpha,(i,j)}(\mathbf{W}) := \tau_\alpha^{(2,\xi)}(\mathbf{W}_{i,j} - \mathbf{W}_{i-1,j}) + \tau_\alpha^{(2,\eta)}(\mathbf{W}_{i,j} - \mathbf{W}_{i,j+1})$$
$$-\tau_\alpha^{(4,\xi)}(\delta_\xi^2\mathbf{W}_{i,j} - \delta_\xi^2\mathbf{W}_{i-1,j}) - \tau_\alpha^{(4,\eta)}(\delta_\eta^2\mathbf{W}_{i,j} - \delta_\eta^2\mathbf{W}_{i,j+1}). \tag{14}$$

The quantities $\tau_\alpha^{(2,\xi)}$ and $\tau_\alpha^{(4,\xi)}$ are cell-based scalings given by the formulae

$$\tau_\alpha^{(2,\xi)} := \frac{\varepsilon^{(2)}}{\Delta t_\alpha} \max_{(i,j)\in\Omega_\alpha} \{\kappa_{i,j}^\xi\}, \tag{15a}$$

$$\tau_\alpha^{(4,\xi)} := \max\left\{0, \frac{\varepsilon^{(4)}}{\Delta t_\alpha} - \tau_\alpha^{(2,\xi)}\right\}, \tag{15b}$$

$$\kappa_{i,j}^\xi = \frac{|\delta_\xi^2 p_{i,j}|}{(4 + \delta_\xi^2)p_{i,j}}, \tag{15c}$$

and $\varepsilon^{(2)}$ and $\varepsilon^{(4)}$ are user chosen constants. Similar quantities are also defined for the $\eta$ coordinate direction. These terms are combined with the cell-based residual terms to give the nodal residual

$$\mathbf{N}_{i,j}(\mathbf{W}) := \frac{\sum_{\alpha=1}^{p} V_\alpha(D_{\alpha,(i,j)}\mathbf{R}_\alpha + A_{\alpha,(i,j)})}{\sum_{\alpha=1}^{p} V_\alpha}. \tag{16}$$

When four cells meet at a common vertex, the overall effect of the distribution of the artificial viscosity vector is to add a scaled second and fourth-difference to the node-based equation (12).

### 5.1. *Analysis of the basic model*

*5.1.1. Cell-based scalings.* An obvious consideration in the design of any artificial dissipation model is its effect on the accuracy of the base discretization scheme being used. When the solution is smooth the artificial dissipation terms should introduce an error of higher order compared to the discretization error of the governing equations. For a second-order scheme like the cell-vertex method this means that the error introduced by the artificial dissipation terms must be at least $O(h^3)$. Examining the scalings (15a) and (15b) we note that both $\tau_\alpha^{(2,\cdot)}$ and $\tau_\alpha^{(4,\cdot)}$ are proportional to $\Delta t_\alpha^{-1}$, which is determined for inviscid problems by a local CFL condition. Since the maximum eigenvalue of the flux Jacobian matrices is always bounded away from zero, $\Delta t_\alpha^{-1}$ is $O(h^{-1})$ and since both $\kappa_{i,j}^{\xi}$ and $\kappa_{i,j}^{\eta}$ are $O(h^2)$ on smoothly varying grids, this implies that $\tau_\alpha^{(2,\cdot)}$ and $\tau_\alpha^{(4,\cdot)}$ are $O(h)$ and $O(h^{-1})$ respectively. When the contributions from the four cells meeting at a node are summed, the error introduced by both the second and fourth-difference artificial dissipation terms is therefore $O(h^3)$. If the exact solution is smooth and the computation is performed on a smoothly varying grid, second-order accuracy of the basic discretization scheme should therefore be observed. Although this analysis shows that the artificial dissipation model does not affect the asymptotic accuracy of the finite volume discretization, it does not give us any insight into the level of artificial dissipation present in a solution on a fixed grid.

We now discuss two deficiencies of the original model that we propose to eradicate. First, since the edge differences in both co-ordinate directions are scaled by the cell-based quantity $\Delta t_\alpha^{-1}$, the above dissipation model is isotropic in nature. This may be acceptable for Euler calculations which are usually performed on grids that have close to unit aspect ratio cells. However, an isotropic scaling of the artificial dissipation terms may introduce excessive dissipation when strongly graded grids are used for high Reynolds number Navier–Stokes calculations. For example, consider calculating flow over a flat plate using rectangular grid cells where $\Delta x \gg \Delta y$. Close to the plate surface the fourth-difference dissipation

$$\frac{\varepsilon^{(4)}}{\Delta t}(\delta_\xi^4 \mathbf{W}_{i,j} + \delta_\eta^4 \mathbf{W}_{i,j}) \approx \varepsilon^{(4)} c\left(\frac{\Delta x}{\Delta y}(\Delta x)^3 \mathbf{w}_{xxxx} + (\Delta y)^3 \mathbf{w}_{yyyy}\right),$$

where $c$ is the local sound speed. Unless the grid is chosen such that $w_x \Delta x \approx w_y \Delta y$, then excessive dissipation, proportional to the cell aspect ratio, will be added in the $x$-direction. This inaccuracy is directly attributed to the scaling of the edge differences by a *cell-based* time step.

Secondly, we note that the original model multiplies the second and fourth-differences by $\Delta t_\alpha^{-1}$ for each component of the equation system and is therefore scalar in nature. This is the main cause of smeared shock profiles and excessive artificial dissipation in boundary layers. For Navier–Stokes calculations a possible strategy for reducing the level of artificial dissipation in boundary layers is simply to scale the normal dissipation by a factor proportional to the local Mach number,[4] where both $\varepsilon^{(2)}$ and $\varepsilon^{(4)}$ were scaled by the factor $\min\{1, M/M_\infty\}$. Unfortunately, as we shall see later, this simple approach is inadequate.

*5.1.2. Boundary conditions.* Artificial dissipation from cells adjacent to domain boundary has to be modified since a second-difference of the conserved variables in the non-body co-ordinate direction is required on the boundary edge. For example, the distribution of $A_{\alpha,(i,0)}$ normal to the boundary $j=0$ requires $\delta_\eta^2 \mathbf{W}_{i,0}$. As in References 4 and 6 we only consider formulations which use points from inside the solution domain and on the boundary. This results in one-sided difference stencils being used to approximate second and fourth-differences normal to the domain boundary.

If we drop the index $i$ for convenience then the boundary procedure used in Reference 4 is simply to set $\delta_\eta^2 \mathbf{W}_0 = 0$ which will be referred to as BC A in Section 7. This boundary procedure results in the differences

$$(\delta_\eta^4 \mathbf{W})_0 \approx G_0 = \mathbf{W}_2 - 2\mathbf{W}_1 + \mathbf{W}_0 \tag{17}$$

and

$$(\delta_\eta^4 \mathbf{W})_1 \approx G_1 = \mathbf{W}_3 - 4\mathbf{W}_2 + 5\mathbf{W}_1 - 2\mathbf{W}_0 \tag{18}$$

being used on the boundary and at the first interior point respectively. As in Swanson and Turkel[9] we consider a local mode analysis based on the Fourier symbol of the above difference stencils to assess their damping characteristics. The symbol of the difference operator in (17) is

$$\hat{G}_0(\theta) = 2\cos\theta(\cos\theta - 1) + 2\mathrm{i}\sin\theta(\cos\theta - 1),$$

where $\theta$ is the product of the wavenumber and the mesh spacing. For long wavelength modes $\theta \approx 0$ and we get the approximation

$$\hat{G}_0(\theta) \approx -\theta^2 - i\theta^3.$$

What is disturbing about this boundary procedure is that it is in fact anti-diffusive for long wavelengths. For high frequency components $\theta = \pm\pi$ we get

$$\hat{G}_0(\pi) = 4.$$

For comparison, the standard fourth-difference stencil

$$(\delta^4 \mathbf{W})_j = \mathbf{W}_{j+2} - 4\mathbf{W}_{j+1} + 6\mathbf{W}_j - 4\mathbf{W}_{j-1} + \mathbf{W}_{j-2}$$

has the symbol

$$\hat{G}_0(\theta) = 4(\cos\theta - 1)^2.$$

For long wavelengths

$$\hat{G}_0(\theta) \approx \theta^4$$

and for short wavelengths

$$\hat{G}_0(\pi) = 16.$$

Therefore, the boundary difference stencil (17) has a quarter of the high frequency damping capabilities of interior stencil and is anti-diffusive for low frequency components. The symbol of the difference operator (18) is

$$\hat{G}_1(\theta) = 2(1 - \cos\theta)(2 - \cos\theta) - 2\mathrm{i}\sin\theta(1 - \cos\theta)$$

and hence

$$\hat{G}_1(\theta) \approx \theta^2 - \mathrm{i}\theta^3$$

for $\theta \approx 0$ and

$$\hat{G}_1(\pi) = 12.$$

At the first interior point we therefore have second-order dissipation for long wavelength modes and reasonable high frequency damping. The combination of these two difference stencils suggests that

the accuracy of the base discretization may be impaired close to the domain boundary. This will be verified numerically in Section 7.

An alternative boundary condition, which has been advocated for turbulent flows by Swanson and Turkel,[11] is to set

$$\delta_\eta^2 \mathbf{W}_{i,0} = \delta_\eta^2 \mathbf{W}_{i,1}. \tag{19}$$

This results in no normal fourth-difference dissipation being applied at $j=0$. This might appear at first to be unwise as no damping occurs in the normal direction at the boundary. However, this is an improvement on the anti-diffusive effect of BC A. At $j=1$ the fourth-difference stencil used is

$$(\delta^4 \mathbf{W})_1 \approx G_1 = \mathbf{W}_3 - 3\mathbf{W}_2 + 3\mathbf{W}_1 - \mathbf{W}_0 \tag{20}$$

which has a Fourier symbol

$$\hat{G}_1(\theta) = \tfrac{1}{2}\theta^4 - \mathrm{i}\theta^3$$

for $\theta \approx 0$ and

$$\hat{G}_1(\pi) = 8.$$

The stencil (20) is therefore fourth-order dissipative and has reasonable high frequency damping characteristics. This analysis suggests that this boundary condition has a less deleterious effect on accuracy than BC A and will be referred to as BC B in Section 7.

## 6. MODIFICATIONS OF THE BASIC MODEL

In this section we propose three changes to the original dissipation model which attempt to overcome some of its inaccuracies outlined above.

### *6.1. Edge-based scaling*

In order to develop a dissipation model which is more anisotropic, we consider the following modifications. Again using the notation of Figure 2, the distribution of the artificial dissipation vector from cell $\Omega_\alpha$ to node $(i, j)$ is now given by

$$\begin{aligned} A_{\alpha,(i,j)}(\mathbf{W}) \;:=\; & \tau^{(2,\xi)}_{i-\frac{1}{2},j}(\mathbf{W}_{i,j} - \mathbf{W}_{i-1,j}) + \tau^{(2,\eta)}_{i,j+\frac{1}{2}}(\mathbf{W}_{i,j} - \mathbf{W}_{i,j+1}) \\ & - \tau^{(4,\xi)}_{i-\frac{1}{2},j}(\delta_\xi^2 \mathbf{W}_{i,j} - \delta_\xi^2 \mathbf{W}_{i-1,j}) - \tau^{(4,\eta)}_{i,j+\frac{1}{2}}(\delta_\eta^2 \mathbf{W}_{i,j} - \delta_\eta^2 \mathbf{W}_{i,j+1}). \end{aligned} \tag{21}$$

The *edge-based* scaling $\tau^{(2,\xi)}_{i-\frac{1}{2},j}$ is given by

$$\tau^{(2,\xi)}_{i-\frac{1}{2},j} = \varepsilon^{(2)} dl_t \lambda^\xi_{i-\frac{1}{2},j} \Phi^\xi_{i-\frac{1}{2},j}, \tag{22}$$

where

$$dl_t = \frac{V_\alpha + V_\beta}{2|\mathbf{x}_{i,j} - \mathbf{x}_{i-1,j}|},$$

and

$$\Phi^\xi_{i-\frac{1}{2},j} = \max\{\kappa^\xi_{i-2,j}, \kappa^\xi_{i-1,j}, \kappa^\xi_{i,j}, \kappa^\xi_{i+1,j}\}.$$

Here, $\lambda^{\xi}_{i-\frac{1}{2},j}$ is the largest eigenvalue in modulus of the Jacobian matrix $\vec{A}(\mathbf{w},\mathbf{n}) = n_1A(\mathbf{w}) + n_2B(\mathbf{w})$, where $\mathbf{n}=(n_1, n_2)$ is a unit vector in the direction from grid point $(i-1, j)$ to $(i, j)$. For the Euler equations, the largest eigenvalue is given by

$$\lambda^{\xi}_{i-\frac{1}{2},j} = |\mathbf{q}_n| + c, \tag{23}$$

where

$$\mathbf{q}_n = n_1\left(\frac{u_{i,j}+u_{i-1,j}}{2}\right) + n_2\left(\frac{v_{i,j}+v_{-1,j}}{2}\right) \tag{24}$$

and

$$c = \frac{c_{i,j}+c_{i-1,j}}{2}. \tag{25}$$

For $\tau^{(4,\xi)}_{i-\frac{1}{2},j}$ we set

$$\tau^{(4,\xi)}_{i-\frac{1}{2},j} = dl_t\lambda^{\xi}_{i-\frac{1}{2},j}\max[0, \varepsilon^{(4)} - \sigma\Phi^{\xi}_{i-\frac{1}{2},j}], \tag{26}$$

where $\sigma$ is a user defined constant. Similar expressions are used for the scalings in the $\eta$ co-ordinate direction. In Section 7 this dissipation model will simply be called the anisotropic scalar model. The edge-based scalings result in an artificial dissipation model which is similar to Jameson's original model and introduces the eigenvalues of the flux Jacobian matrices much more explicitly which allows us to consider a second modification.

### 6.2. *Matrix-based dissipation*

*6.2.1. Shock-capturing dissipation.* It is well known from symmetric formulations that flux-vector split and flux-difference split upwind schemes can be written as a central discretization plus a matrix-scaled dissipative flux.[8,11] As upwind schemes are designed to capture shocks sharply it seems reasonable to develop an artificial dissipation model which makes a central discretization behave like an upwind scheme at shocks. The shock-capturing component of the basic model is an inexpensive attempt to model a first-order upwind scheme at shocks using a scalar to multiply the shock capturing dissipation. However, improved shock-capturing capabilities can be achieved using a matrix-scaled dissipative flux. Here we replace the scalar $\lambda_{i-\frac{1}{2},j}$ in (6.2) by the matrix $|\vec{A}_{i-\frac{1}{2},j}|$ suggested by a symmetric formulation of Roe's method.[14] More precisely,

$$|\vec{A}_{i-\frac{1}{2},j}| = R|\Lambda|L,$$

where $R$ and $L$ are right and left eigenvector matrices of the linear combination of the flux matrices $\vec{A} = k_1A(\mathbf{w})+k_2B(\mathbf{w})$ and $\mathbf{k}=(k_1, k_2)$ is a unit vector. In this paper the diagonalisation direction is chosen to be from grid node $(i-1, j)$ to grid node $(i, j)$, although the shock normal direction may be more appropriate for shocks that are not grid aligned. The diagonal matrix

$$\Lambda = \mathrm{diag}(\lambda_i)_{i=1,\ldots,4} = \mathrm{diag}(q_{\mathbf{k}}, q_{\mathbf{k}}, q_{\mathbf{k}}+c, q_{\mathbf{k}}-c),$$

where $q_{\mathbf{k}} = k_1u+k_2v$. The elements of the matrices $R$, $L$ and $\Lambda$ are all calculated using Roe's parameter vector. In practice, one has to be careful using the matrix $|\vec{A}|$ scaling, since Roe's scheme allows non-physical expansion shocks to arise at sonic points which are insufficiently damped by the Lax–Wendroff second-order terms. This can easily be remedied by a so called 'entropy fix' where we take $|\lambda_i| = \max(|\lambda_i|, \delta|\lambda_{\max}|)$ where $\delta > 0$ is a chosen (small) parameter. Note that with $\delta = 1$ we recover the scalar model.

*6.2.2. Background smoothing.* The role of fourth-difference background smoothing is to damp high frequency solution components. Proper damping of these frequencies is essential for the successful application of a multigrid method to improve convergence to a steady state. The scaling used in (26) can be motivated by writing a second-order upwind method as a central discretization plus a matrix scaling of fourth differences.[8] Instead of using an appropriate matrix scaling, Jameson's original model multiplies the fourth differences by a scalar quantity. However, it has been shown that this scaling of fourth-differences introduces excessive normal dissipation for high Reynolds number Navier–Stokes calculations.[10] As with the shock capturing dissipation we consider replacing $\lambda_{i-1/2,j}$ in (26) by the matrix scaling $|A_{i-1/2,j}|$. For Roe's method the action of the numerical dissipation vanishes for waves when their wave speeds tend to zero. This appears to be crucial to modelling boundary layers accurately with upwind methods.[15]

The combination of matrix scaling for both the second-difference terms will be investigated in Section 7 where it will be referred to as the matrix-scaled model.

### *6.3. Shock-detection*

In both the scalar and matrix-scaled dissipation models outlined above, a second-difference of pressure is used as a sensor to detect shocks. However, a second-difference in pressure can be large in regions other than at shocks, for example where a shock impinges on a boundary layer or around the leading edge of an aerofoil. The addition of second-difference shock-capturing dissipation in these regions can adversely effect accuracy. There are many choices of switching function which can be made to distinguish more clearly between a shocked and non-shocked region. For example, Hall[16] uses a third difference of density and Swanson and Turkel[11] have considered using an entropy like variable which is further scaled by the local Mach number. Here, we consider using the simple normal shock-detection procedure of Crumpton and Shaw.[17] The algorithm produces a cell-based switch, $S_\alpha$, that takes a unit value when a shock passes through the cell $\Omega_\alpha$ and zero elsewhere (see Reference 17 for the exact details). The coefficients $\kappa^\xi$ and $\kappa^\eta$ are then scaled by $S_\alpha$. This ensures that the second-difference dissipation is only switched on where it is required.

## 7. NUMERICAL EXPERIMENTS

In this section we investigate the effects of the modifications of the original dissipation model given above by considering three test cases. The various constants for both the scalar and matrix-based artificial dissipation model are shown in Table I. These constants were calibrated on the transonic Euler test given in the next subsection with the requirement of sharp shock resolution. These same constants were then used for a Navier–Stokes problem.

### *7.1. Transonic Euler flow over a NACA0012 aerofoil*

To test the shock-capturing capability of the matrix-based dissipation, we consider inviscid transonic flow over a NACA0012 aerofoil. The freestream flow conditions are $M_\infty = 0{\cdot}8$ at an angle of attack of 1·25°, which results in a strong shock on the upper surface of the aerofoil and a much

Table I. Artificial dissipation constants for both Euler and Navier–Stokes test cases

| Dissipation model | $\varepsilon^{(2)}$ | $\varepsilon^{(4)}$ | $\sigma$ | $\delta$ |
|---|---|---|---|---|
| Scalar | 4·0 | 0·05 | 2·0 | N/A |
| Matrix | 20·0 | 0·05 | 2·0 | 0·05 |

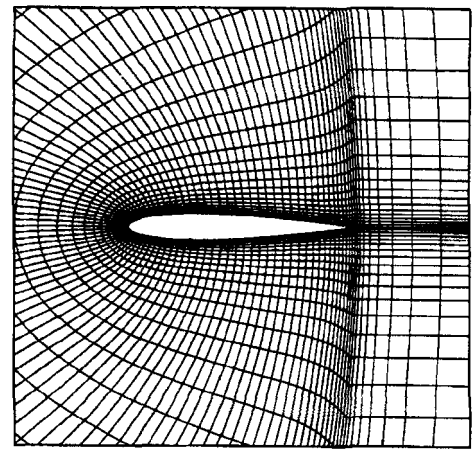

Figure 3. 129 × 33 C-grid used for transonic Euler calculations over a NACA0012 aerofoil

weaker shock on the lower surface. Three C-type grids were used in this study. The finest grid has 513 by 129 nodes with 386 nodes on the aerofoil surface, and extends 15 chord lengths into the far-field. Two coarser grids with 265 × 65 and 129 × 33 nodes, were obtained by omitting every other point of the next finer grid. A general view of the 129 × 33 grid is shown in Figure 3. Close ups of the leading edge regions of the three grids are shown in Figure 4, where we can see the clustering of the cells into the stagnation point.

We first consider the effect of the shock detection procedure on the generation of spurious entropy at the leading edge of the aerofoil. Figure 5 confirms that additional dissipation is added with the standard pressure-based shock detector which is not present when we use the shock detection procedure. This can most clearly be seen from the balance of the mass conservation nodal residual. Figure 6 shows the results around the leading edge using BC B and shock detection. As predicted in the analysis earlier there is a substantial reduction in artificial dissipation present on the aerofoil surface using this boundary condition. We can also see for this figure that matrix-scaling at this smooth part of the flow has a comparable effect to that of the scalar dissipation.

Figure 7 shows contour plots of pressure coefficient, surface line plots of pressure coefficient and surface line plots of entropy deviation for the three grids using the scalar, anisotropic model with shock-detection and BC B. On the coarsest grid the upper shock has been captured within four mesh cells and spurious entropy has been generated at the leading edge. As the grid is refined there is a

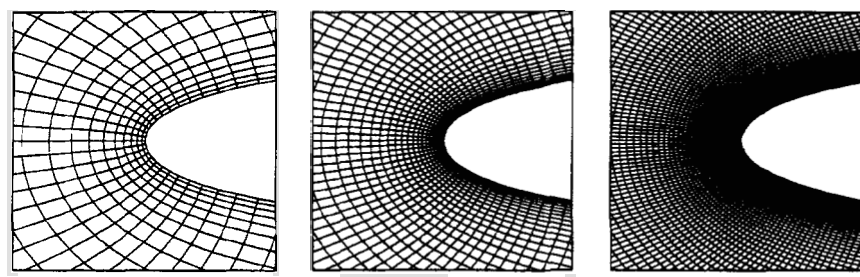

(a) (b) (c)

Figure 4. Close up of leading edge region of (a) 129 × 33; (b) 257 × 65; (c) 513 × 129 node grids used for transonic Euler calculations

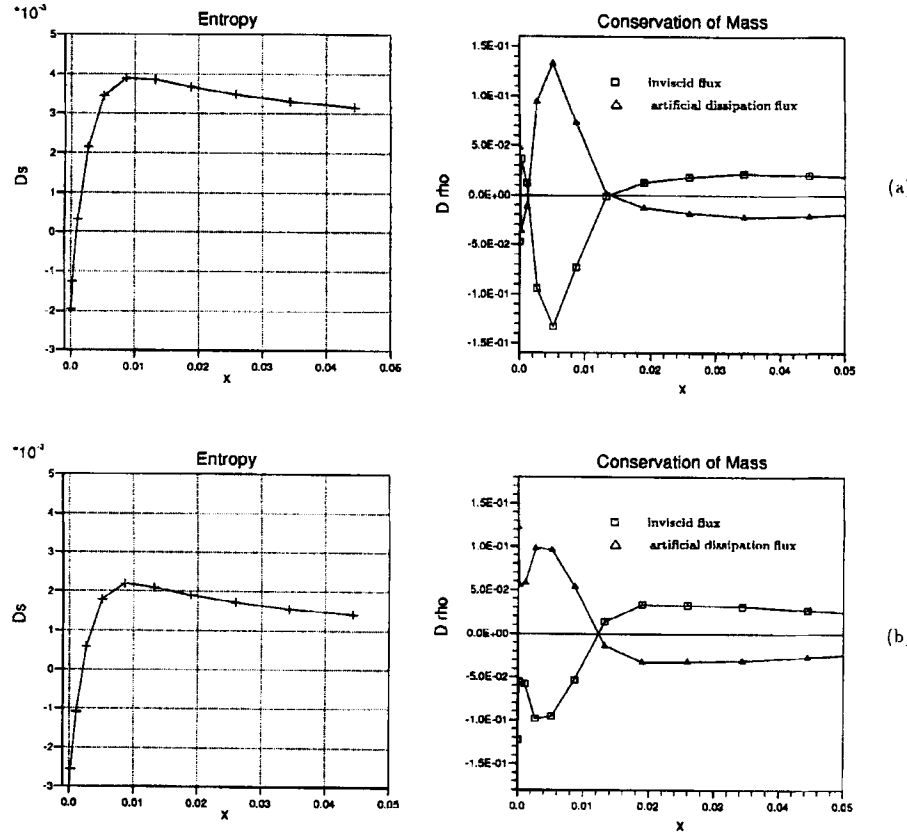


Figure 5. Entropy plot and budget plot of mass conservation equation on the upper surface of NACA0012 aerofoil using BC A; (a) without shock detection (b) with shock detection

Table II. Computed drag, lift and moment coefficients for scalar dissipation with shock-detection for Euler test case $M_\infty = 0{\cdot}8$ and $\alpha = 1{\cdot}25°$

| Mesh | CD | CL | CM |
|---|---|---|---|
| 129 × 33 | 0·02243 | 0·36026 | −0·03992 |
| 265 × 65 | 0·02260 | 0·35972 | −0·03960 |
| 513 × 129 | 0·02250 | 0·36015 | −0·03953 |

Table III. Computed drag, lift and moment coefficients for matrix dissipation with shock-detection for Euler test case $M_\infty = 0{\cdot}8$ and $\alpha = 1{\cdot}25°$

| Mesh | CD | CL | CM |
|---|---|---|---|
| 129 × 33 | 0·02246 | 0·36182 | −0·04013 |
| 265 × 65 | 0·02261 | 0·36000 | −0·03962 |
| 513 × 129 | 0·02254 | 0·36044 | −0·03970 |

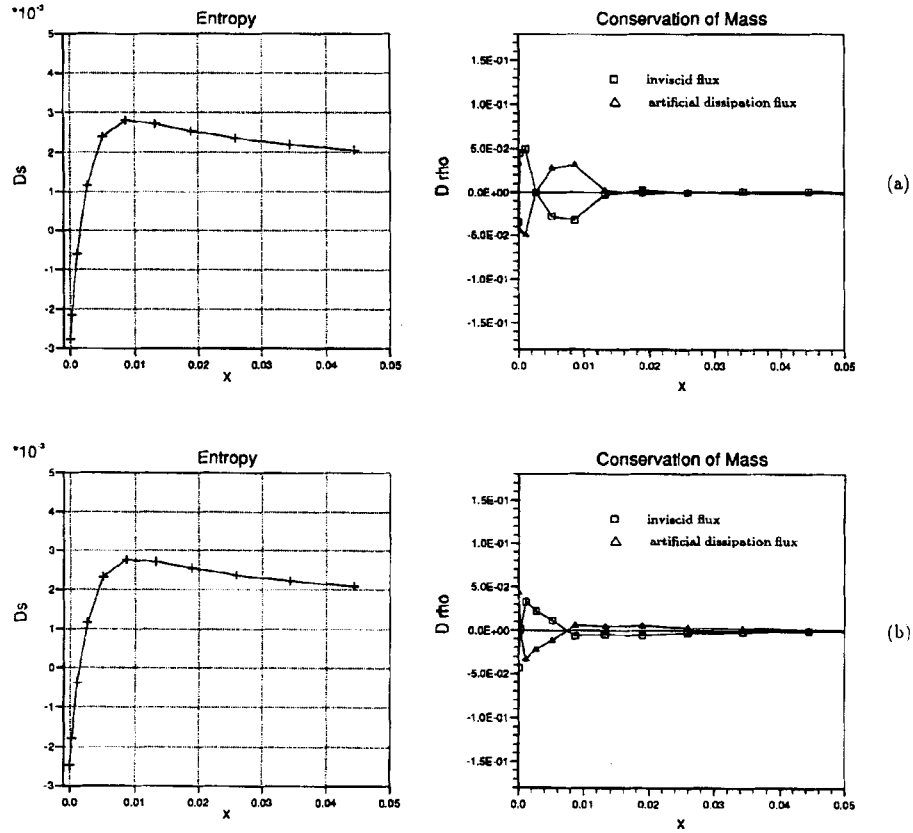


Figure 6. Entropy plot and budget plot of mass conservation equation on the upper surface of NACA0012 aerofoil using BC B and shock detection; (a) scalar-scaling (b) matrix-scaling

marked improvement in the resolution of the lower shock and a reduction of spurious entropy generation at the leading edge. However, even on the finest grid the upper shock is smeared over four cell widths.

Table II shows the computed lift, drag and moment coefficients for the three grids, all of which were obtained using the far-field vortex correction boundary condition of Thomas and Salas.[18] It is clear from this table that finer grids are required than those used here to determine the rate of convergence of the method. The results for all three grids are remarkably similar and differ by less than 1%.

Figure 8 shows the corresponding results using the matrix-based dissipation model. The computed shock profiles on the upper and lower surface are sharper than those predicted with the scalar dissipation model. In addition we note that the matrix model behaves similarly to the scalar model in smooth regions of the flow. Table III shows the lift, drag and moment coefficients which behave in a similar fashion to those for the scalar model. Again, finer grids would be necessary to investigate the convergence rate of the method.

### *7.2. Subsonic laminar flow over a flat plate*

The second test case considered is subsonic, laminar, viscous flow over a semi-infinite flat plate at zero angle of attack with $M_\infty = 0{\cdot}8$ and $Re = 2{\cdot}96 \times 10^5$. The domain for this problem is the

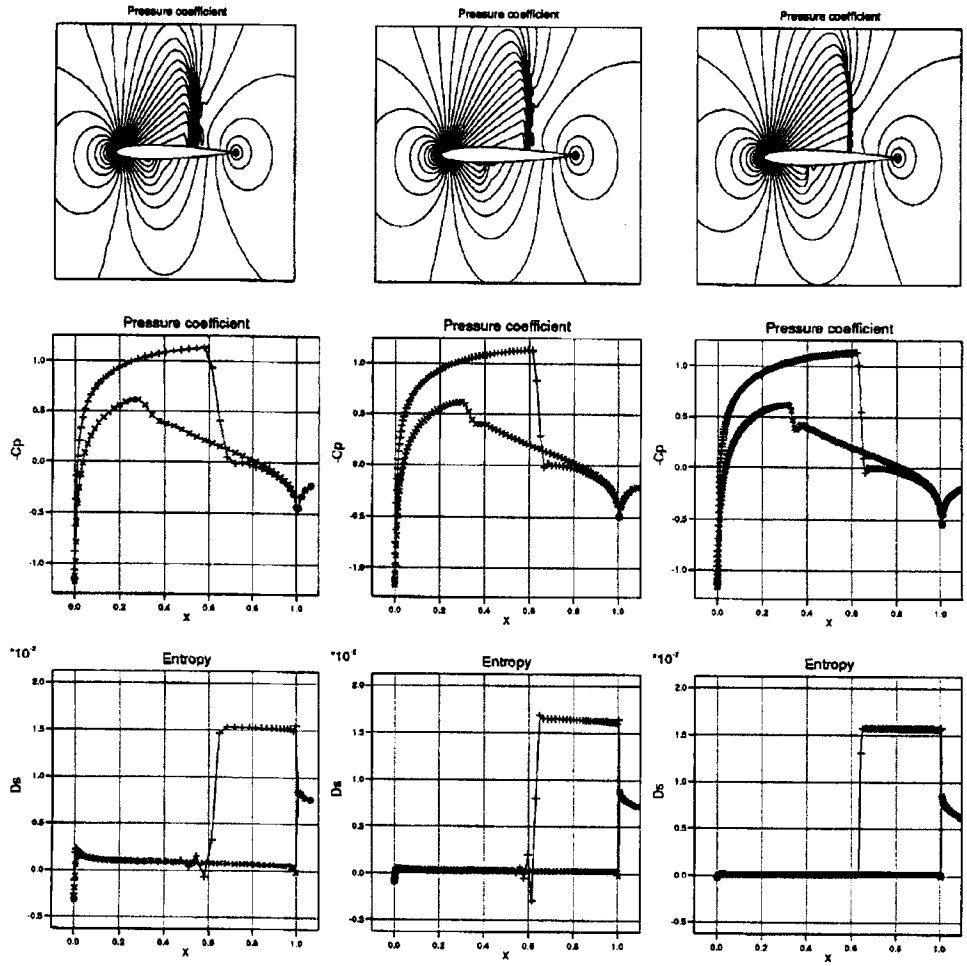


Figure 7. Plots of pressure contours, pressure coefficient and entropy deviation on (a) 129 × 33; (b) 257 × 65; and (c) 513 × 129 node grids with $M_\infty = 0{\cdot}8$, $\alpha = 1{\cdot}25°$ using scalar dissipation with shock-detection

Table IV. Drag coefficient and number of iterations taken to reach convergence for viscous flow over a flat plate

| Dissipation model | Avis BC | CD | Iterations |
|---|---|---|---|
| Scalar | A | 0·002882 | 14000 |
| Scalar | B | 0·003215 | 15000 |
| Scalar, Mach Scaled | B | 0·003131 | 15900 |
| Matrix | B | 0·003288 | 17750 |

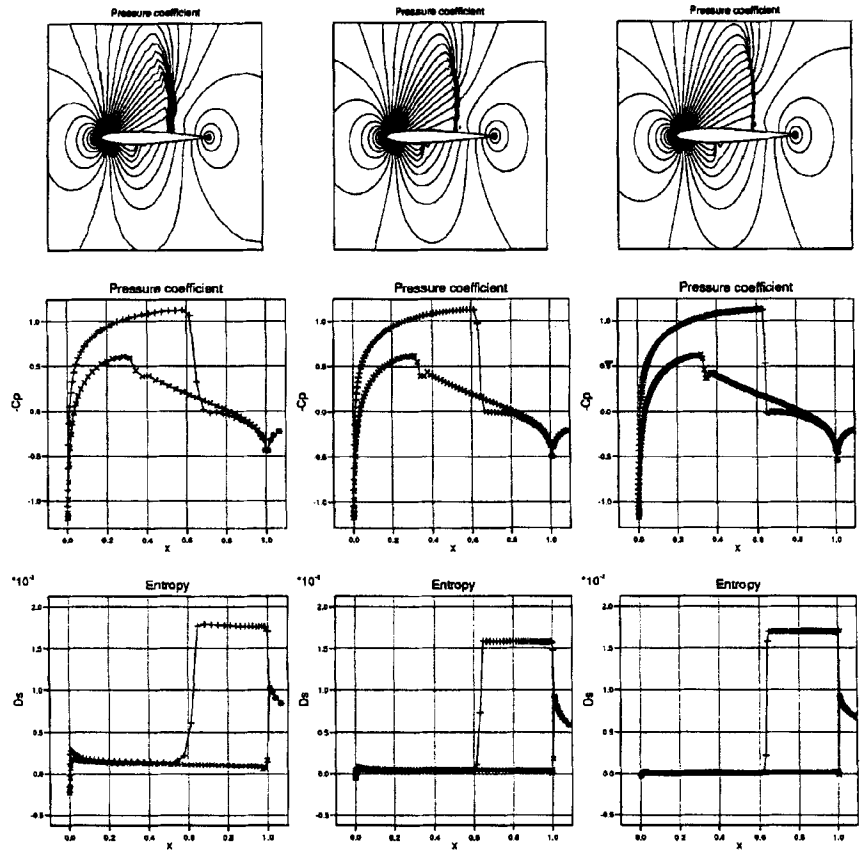


Figure 8. Pressure coefficient contours, pressure coefficient and entropy deviation on (a) 129 × 33; (b) 257 × 65; and (c) 513 × 129 node grids with $M_\infty = 0{\cdot}8$, $\alpha = 1{\cdot}25°$ using matrix dissipation with shock-detection

rectangular region $(-0{\cdot}25, 2) \times (0, 1{\cdot}5)$ and the plate is introduced along the bottom of the domain at $x = 0$. The computational grid has 73 × 81 nodes, is uniform in the $x$-direction and is stretched in the $y$-direction towards the plate. Therefore, no attempt has been made to model the flow accurately at the plate leading edge.

Figure 9(a) shows the computed skin-friction coefficient along the plate using the anisotropic, scalar dissipation model with artificial dissipation boundary condition A. The cell-vertex solution badly underestimates the reference Blasius solution towards the front of the plate suggesting the presence of excessive numerical dissipation in this region. Figure 9(b) shows the tangential velocity profile at $x = 1$, which is plotted with respect to the similarity co-ordinate $\eta = y\sqrt{Re/x}$. Compared to the Blasius profile we see that the boundary layer is excessively thick and has an overshoot at its edge. This again suggests excessive artificial dissipation.

To investigate the level of artificial dissipation present in a numerical solution we consider the balance of the inviscid, viscous and artificial dissipation fluxes of the nodal residual. Figure 10(a) shows the balance of the three flux contributions through the boundary layer for the $x$-momentum and mass conservation nodal residuals at $x = 1$. We see that the artificial dissipation flux is significant close to the surface of the plate, throughout the boundary layer and at the boundary layer edge. Similar plots have been obtained by Allmaras[10] and Tattersall and McGuirk.[19] As the flow is

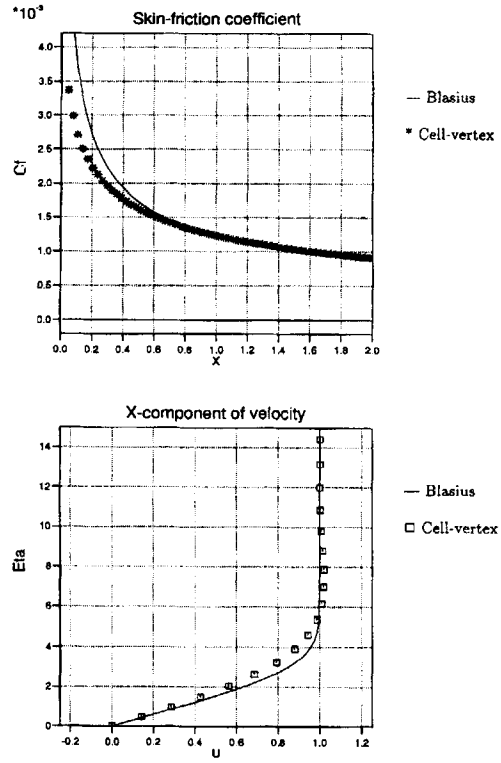


Figure 9. Skin-friction coefficient along plate and tangential velocity at x = 1 for Navier–Stokes flow over a flat plate, $Re = 2{\cdot}96 \times 10^5$ and $M_\infty = 0{\cdot}8$, using anisotropic scalar dissipation with boundary condition A

subsonic, the excessive dissipation in the solution is caused by the fourth-difference dissipation. As mentioned earlier, the role of the Lax–Wendroff distribution matrices is to provide a mapping from the cell residuals to the nodal residuals. At the steady state the nodal residuals are zero and we hope that the cell residuals have also been set to zero. Figure 10(b) shows the inviscid and viscous flux contributions to the $x$-momentum and mass conservation cell residuals. These figures indicate a very poor cell flux balance that has been mainly caused by excessive numerical dissipation. Both the cell and nodal flux balances are especially poor close to the plate surface which suggests an inaccuracy caused by the artificial dissipation boundary condition. Figures 11 and 12 show the results using the artificial dissipation boundary condition B. The results are considerably more accurate at the plate surface which is clearly evident from the skin-friction coefficient. Furthermore, there is a ten-fold reduction in the level of artificial dissipation in the mass conservation nodal residual and a two-fold reduction in the mass conservation cell residual. All of the following results were therefore obtained using this boundary condition for the fourth-difference dissipation.

The effect of scaling the fourth-difference dissipation normal to the plate surface by the local Mach number is shown in Figures 13 and 14. This clearly leads to an improvement of the computed skin-friction coefficient along the plate but the nodal and cell equation budget plots only show a limited improvement. In particular, there is still an excessive amount of dissipation at the boundary layer edge which has been unaffected by the Mach number scaling.

Finally, Figures 15 and 16 show the results obtained using the matrix scaling of the fourth-difference dissipation. The computed skin-friction coefficient is accurately predicted along the length of the plate, in particular at the leading edge. The improvement in the solution is more clearly seen

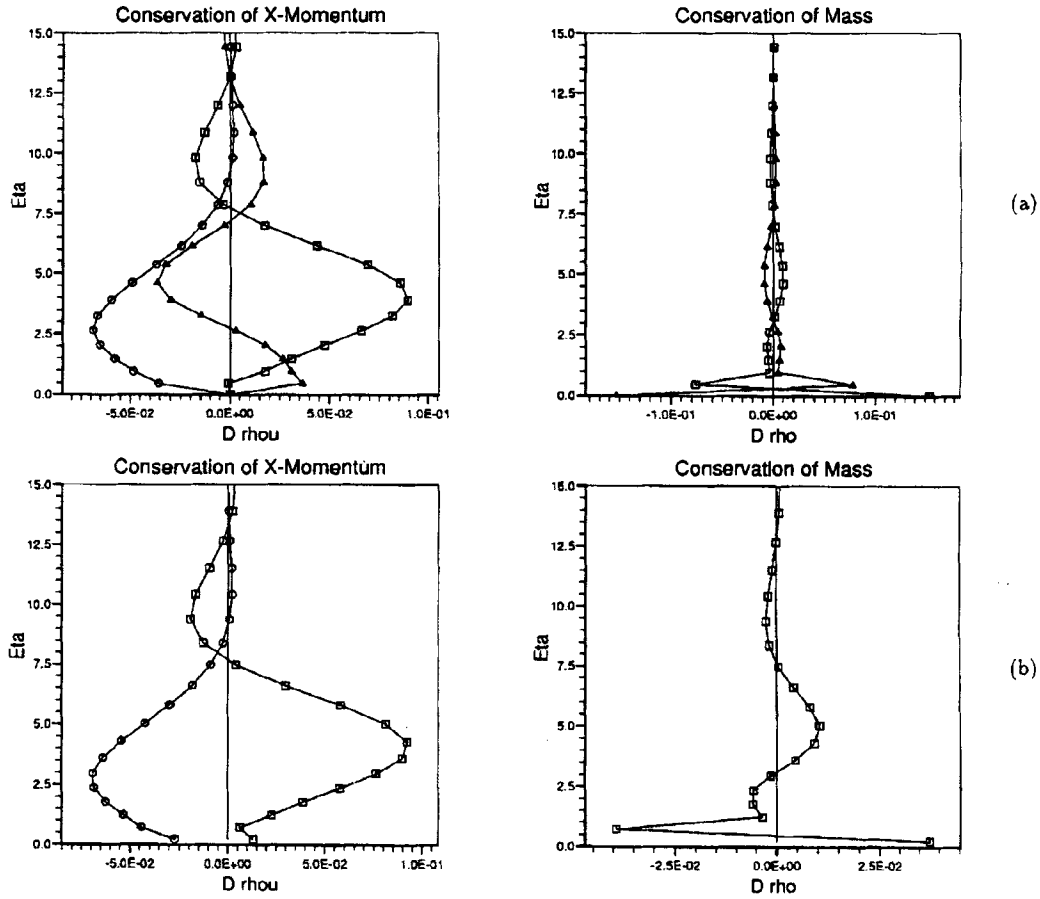


Figure 10. Budget plots of $x$-momentum and mass conservation equations at x = 1 for the (a) nodal residual and (b) cell residual for Navier–Stokes flow over a flat plate, $Re = 2{\cdot}96 \times 10^5$ and $M_\infty = 0{\cdot}8$, using anisotropic scalar dissipation with boundary condition A

when we look at the tangential velocity profile which has very little overshoot and resembles the Blasius profile more closely. In addition, the nodal and cell budget plots both show a dramatic reduction in the level of fourth-difference dissipation.

Table IV shows the computed drag coefficient and the number of iterations to reach convergence for all of the above dissipation models. As expected, the matrix model takes longer to converge than all of the variations of the scalar model due to its reduced damping capabilities. However, this is outweighed by the improvement in accuracy which is evident from the plots given above.

## 8. CONCLUSIONS

In this paper we have investigated an artificial dissipation model for use with the cell-vertex finite volume discretization of the Euler and Navier–Stokes equations. The numerical results obtained for Euler aerofoil calculations show that the model improves shock resolution and reduces the level of spurious entropy generation at the aerofoil leading edge. For Navier–Stokes calculations the amount of excessive numerical dissipation has been reduced thus increasing the accuracy of the prediction of

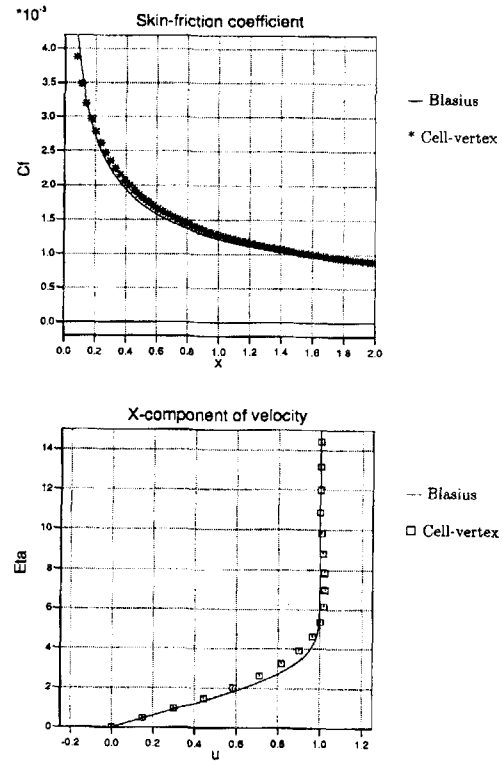


Figure 11. Skin-friction coefficient along plate and tangential velocity at $x = 1$ for Navier–Stokes flow over a flat plate, $Re = 2{\cdot}96 \times 10^5$ and $M_\infty = 0{\cdot}8$, using anisotropic scalar dissipation with boundary condition B

boundary layer thickness and viscous drag. The decrease in artificial dissipation within boundary layers also helps to attain a better flux balance on the primary grid cells. The decrease in the level of fourth-difference dissipation does increase slightly the number of iterations needed to reach a converged solution and with each iteration being slightly more expensive the overall effect is to increase the cost of a typical calculation by 20%. However, the improvement in accuracy, especially on coarse grids, makes the use of the matrix dissipation worthwhile. Finally, although a particular cell-vertex scheme was used in this study, the matrix-dissipation model with shock-detection can also be used with other centred vertex-based finite volume methods. The analysis of the artificial dissipation boundary conditions is also applicable for such schemes.

ACKNOWLEDGEMENTS

I thank Professor K. W. Morton and Dr P. I. Crumpton for advice and many helpful discussions. Funding of part of this work was provided by the Defence Research Agency, Farnborough, U.K.

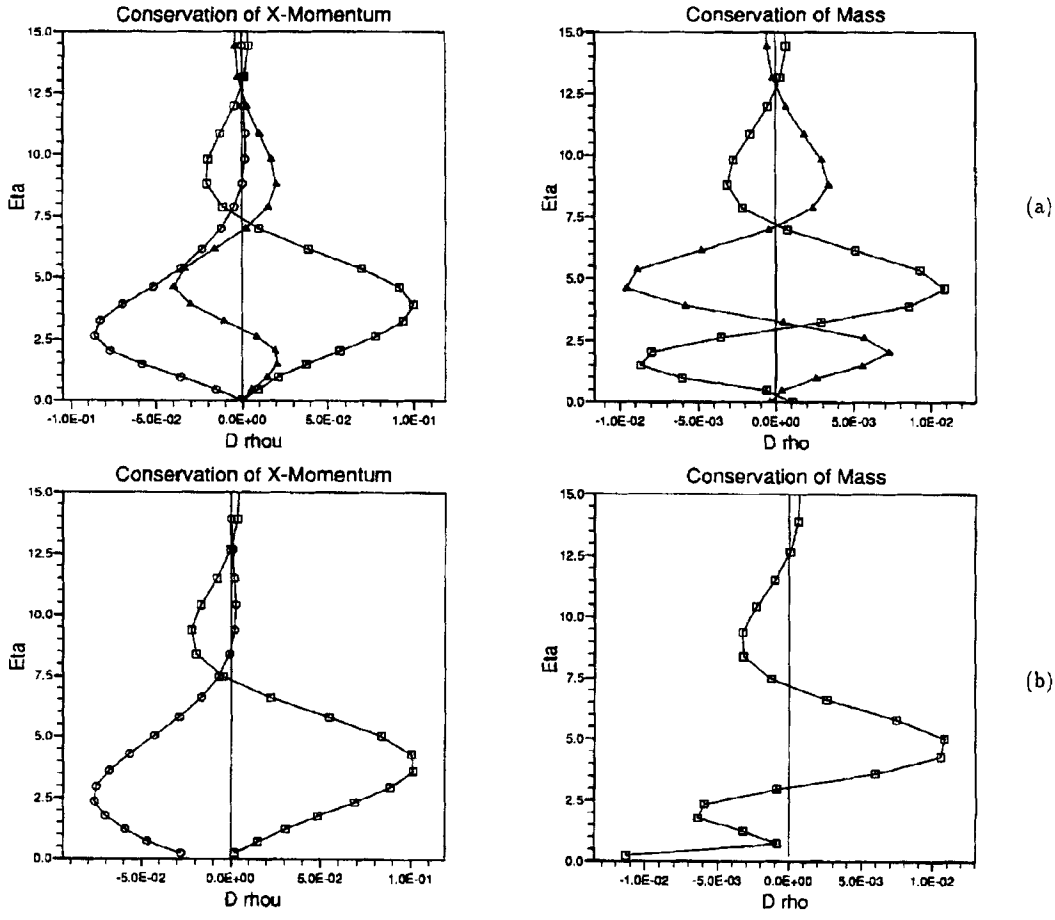


Figure 12. Budget plots of $x$-momentum and mass conservation equations at x = 1 for the (a) nodal residual and (b) cell residual for Navier–Stokes flow over a flat plate, $Re = 2{\cdot}96 \times 10^5$ and $M_\infty = 0{\cdot}8$, using anisotropic scalar dissipation with boundary condition B

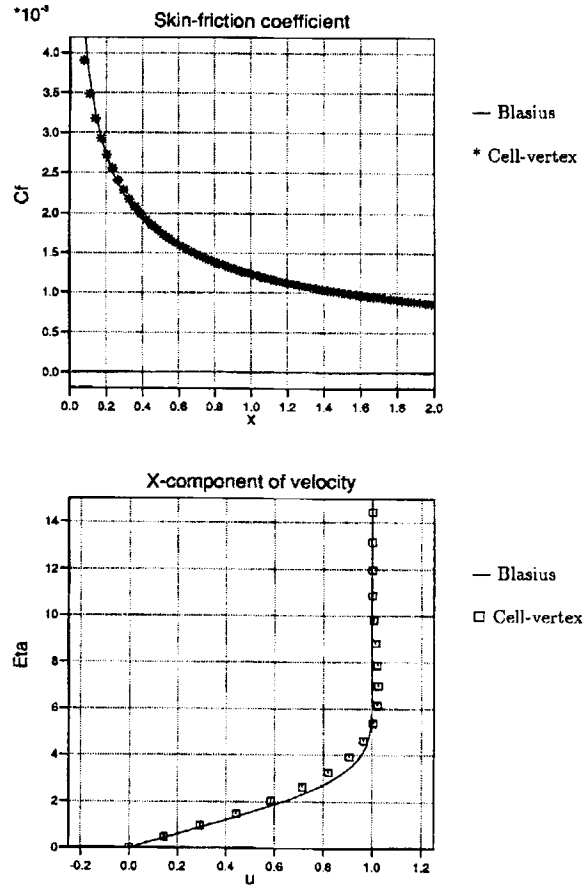


Figure 13. Skin-friction coefficient along plate and tangential velocity at $x = 1$ for Navier–Stokes flow over a flat plate, $Re = 2{\cdot}96 \times 10^5$ and $M_\infty = 0{\cdot}8$, using anisotropic scalar dissipation with Mach scaling and boundary condition B

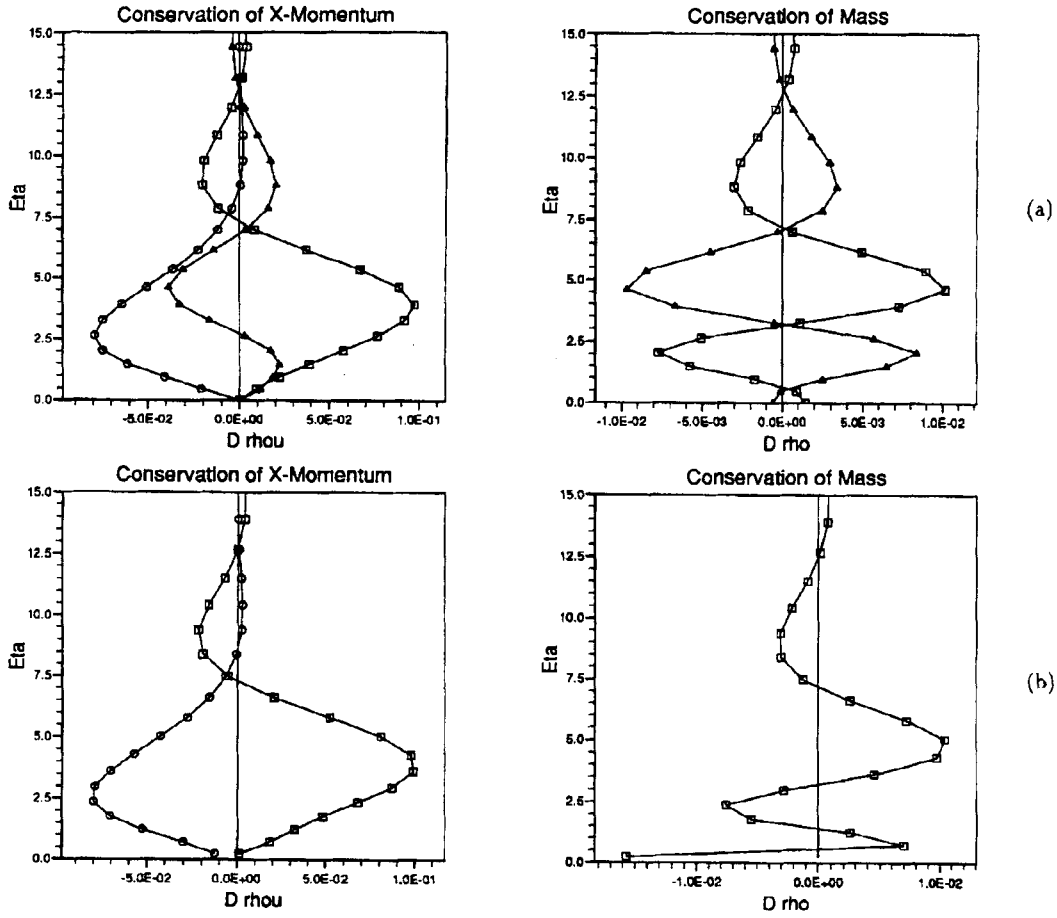


Figure 14. Budget plots of $x$-momentum and mass conservation equations at x = 1 for the (a) nodal residual and (b) cell residual for Navier–Stokes flow over a flat plate, $Re = 2{\cdot}96 \times 10^5$ and $M_\infty = 0{\cdot}8$, using anisotropic scalar dissipation with Mach scaling and boundary condition B

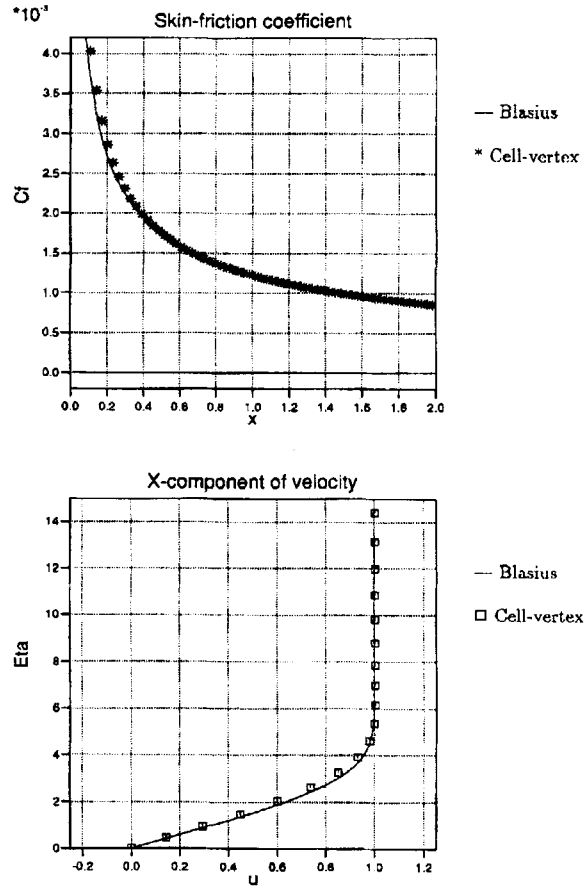


Figure 15. Skin-friction coefficient along plate and tangential velocity at $x = 1$ for Navier–Stokes flow over a flat plate, $Re = 2{\cdot}96 \times 10^5$ and $M_\infty = 0{\cdot}8$, using anisotropic matrix dissipation and boundary condition B

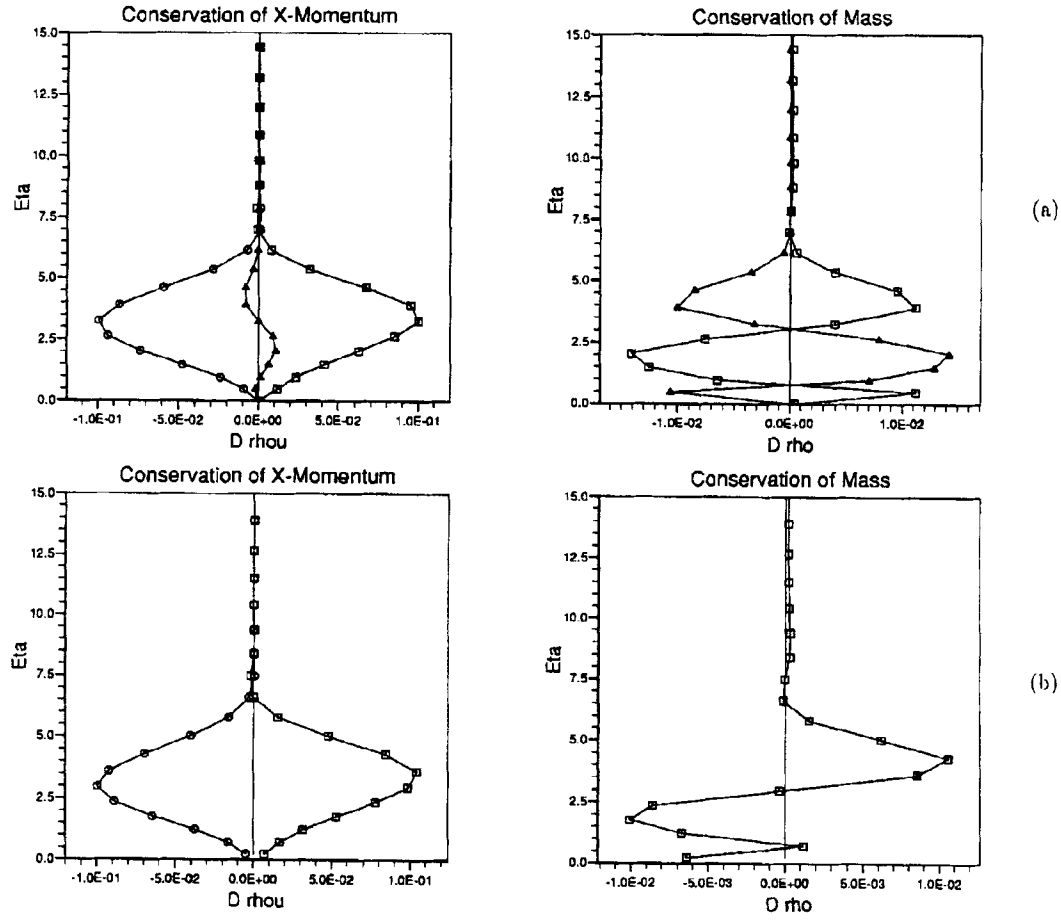


Figure 16. Budget plots of $x$-momentum and mass conservatin equations at x = 1 for the (a) nodal residual and (b) cell residual for Navier–Stokes flow over a flat plate, $Re = 2{\cdot}96 \times 10^5$ and $M_\infty = 0{\cdot}8$, using anisotropic matrix dissipation with boundary condition B

## REFERENCES


1. R. H. Ni, 'A multiple grid method for solving the Euler equations.' *AIAA J.*, **20**, 1565–1571 (1982).
2. M. G. Hall, 'Cell-vertex multigrid schemes for the solution of the Euler equations', in K. W. Morton and M. J. Baines, editors, *Numerical Methods for Fluid Dynamics II*, pp. 303–345. Oxford University Press, 1986.
3. K. W. Morton and M. F. Paisley, 'A finite volume scheme with shock fitting for the steady Euler equations'. *J. Comp. Phys.*, **80**, 168–203 (1989).
4. P. I. Crumpton, J. A. Mackenzie, and K. W. Morton, 'Cell vertex algorithms for the compressible Navier–Stokes equations'. *J. Comput. Phys.*, **109**, 1–155 (1993).
5. P. I. Crumpton, J. A. Mackenzie, and K. W. Morton, 'A consistence cell vertex finite volume method for the compressible Navier–Stokes equations'. In M. Napolitano and F. Sabetta, editors, *Lecture Notes in Physics*, vol. 414, pp. 519–523. Springer-Verlag, 1993.
6. K. W. Morton, P. I. Crumpton, and J. A. Mackenzie, 'Cell vertex methods for inviscid and viscous flows', *Computers Fluids*, **22**, 91–102 (1993).
7. A. Jameson, W. Schmidt, and E. Turkel, Numerical solutions of the Euler equations by finite volume methods using Runge-Kutta time stepping. AIAA Paper 81-1259, 1981.
8. T. H. Pulliam, Artificial dissipation models for the Euler equations. *AIAA J.*, **24**, 1931–1940 (1986).
9. R. C. Swanson and E. Turkel, Artificial dissipation and central difference schemes for the Euler and Navier–Stokes equations. AIAA Paper No. 87-1107, 1987.
10. S. R. Allmaras, Contamination of laminar boundary layers by artificial dissipation in Navier–Stokes solutions. In K. W. Morton and M. J. Baines, editors, *Numerical Methods in Fluid Dynamics V*. Oxford University Press, 1995.
11. R. C. Swanson and E. Turkel, On central-difference and upwind schemes. ICASE Report No. 90-44, 1990.
12. J. W. van der Burg, J. G. M. Kuerten, and P. J. Zandbergen, 'Improved shock-capturing of Jameson's scheme for the Euler equations'. *Int. J. Numer. Methods Fluids*, **15**, 649–671 (1992).
13. K. W. Morton, M. A. Rudgyard, and G. J. Shaw, 'Upwind iteration methods for the cell vertex scheme in one dimension'. Technical Report NA91/09, Oxford University Computing Laboratory, 11 Keble Road, Oxford, OX1 3QD, 1991.
14. P. L. Roe, 'Approximate Riemann solvers, parameters vectors, and difference schemes'. *J. Comput. Phys.*, **43**, 357–372 (1981).
15. B. Van Leer, J. L. Thomas, P. Roe, and R. W. Newsome, 'A comparison of numerical flux formulas for the Euler and Navier–Stokes equations'. AIAA Paper 87–1104, 1987.
16. M. G. Hall, 'A vertex centroid scheme for improved finite volume solution of the Navier–Stokes equations'. AIAA Paper 91-1540, 1991.
17. P. I. Crumpton and G. Shaw, 'A vertex-centred finite volume method with shock detection'. *Int. J. Numer. Methods Fluids*, **18**, 605–625 (1994).
18. J. L. Thomas and M. D. Salas, 'Far-field boundary conditions for transonic lifting solutions to the Euler equations'. *AIAA J.*, **24**, 1074–1080 (1986).
19. P. Tattersall and J. McGuirk, 'Evaluations of numerical diffusion effects in viscous flow calculations'. *Computers Fluids*, **23**, 177–209 (1994).